Mid-infrared to telecom-band supercontinuum generation in highly nonlinear silicon-on-insulator wire waveguides

Bart Kuyken[1,2*], Xiaoping Liu[3,‡], Richard M. Osgood Jr.[3], Roel Baets[1,2], Günther Roelkens[1,2] and William M. J. Green[4]

[1]*Photonics Research Group, Department of Information Technology, Ghent University – imec, Ghent B-9000, Belgium.*

[2]*Center for Nano- and Biophotonics (NB-Photonics), Ghent University, Ghent, Belgium.*

[3]*Microelectronics Sciences Laboratories, Columbia University, New York, NY 10027, USA.*

[4]*IBM Thomas J. Watson Research Center, 1101 Kitchawan Road, Yorktown Heights, NY 10598, USA.*

[‡]*Current address: OFS Labs, 19 Schoolhouse Road, Somerset, NJ 08873, USA.*

[*]*Bart.Kuyken@intec.ugent.be*

Abstract: We demonstrate the generation of a supercontinuum in a 2 cm long silicon wire by pumping the wire with mid-infrared picosecond pulses in the anomalous dispersion regime. The supercontinuum extends from 1535 nm up to 2525 nm for a coupled peak power of 12.7 W. It is shown that the supercontinuum originates primarily from the amplification of background noise. A detailed analysis of the spectral components which are generated through phase-matched processes is applied to extract the group velocity dispersion and fourth-order dispersion coefficient of the silicon wire waveguide.

OCIS codes: (130.4310) Nonlinear Waveguides; (320.6629) Supercontinuum Generation

References and links

1. C. F. Kaminski, R. S. Watt, A. D. Elder, J. H. Frank and J. Hult, "Supercontinuum radiation for applications in chemical sensing and microscopy," App. Phys. B: Lasers and Optics **92**, 367-378 (2008).
2. I. Hartl, X. D. Li, C. Chudoba, R. K. Ghanta, T. H. Ko, J. G. Fujimoto, J. K. Ranka, and R. S. Windeler, "Ultrahigh-resolution optical coherence tomography using continuum generation in an air–silica microstructure optical fiber," Opt. Lett. **26**, 608-610 (2001).
3. S. V. Smirnov, J. D. Ania-Castanon, T. J. Ellingham, S.M. Kobtsev, S. Kukarin, S.K. Turitsyn "Optical spectral broadening and supercontinuum generation in telecom applications," Opt. Fiber Tech. **12**, 122-147 (2006).
4. W. J. Wadsworth, A. Ortigosa-Blanch, J. C. Knight, T. A. Birks, T.-P. Martin Man, and P. St. J. Russell, "Supercontinuum generation in photonic crystal fibers and optical fiber tapers: a novel light source," J. Opt. Soc. Am. B **19**, 2148-2155 (2002).
5. J. M. Dudley, G. Gently, S. Coen, "Supercontinuum generation in photonic crystal," Rev. of Mod. Phys. **78**, 1135-1184 (2006).
6. A. V. Husakou and J. Herrmann, "Supercontinuum Generation of Higher-Order Solitons by Fission in Photonic Crystal Fibers," Phys. Rev. Lett. **87**, 203901 (2001).
7. M. R. Lamont, B. Luther-Davies, D. Y. Choi, S. Madden, and B. J. Eggleton, "Supercontinuum generation in dispersion engineered highly nonlinear (γ = 10 /W/m) As_2S_3 chalcogenide planar waveguide," Opt. Express **16**, 14938-14944 (2008).
8. R. Halir, Y. Okawachi, J. S. Levy, M. A. Foster, M. Lipson, A. L. Gaeta, "Octave Spanning Supercontinuum Generation in CMOS Compatible Silicon Nitride Waveguides," in CLEO, PDPA6 (2011).
9. D. Duchesne, M. Peccianti, M. R. E. Lamont, M. Ferrera, L. Razzari, F. Légaré, R. Morandotti, S. Chu, B. E. Little, and D. J. Moss, "Supercontinuum generation in a high index doped silica glass spiral waveguide," Opt. Express **18**, 923-930 (2010).
10. I.-W. Hsieh, X. Chen, X. Liu, J. I. Dadap, N. C. Panoiu, C.-Y. Chou, F. Xia, W. M. Green, Y. A. Vlasov, and R. M. Osgood Jr., "Supercontinuum generation in silicon photonic wires," Opt. Express **15**, 15242-15249 (2007).
11. R. M. Osgood Jr., N. C. Panoiu, J. I. Dadap, X. Liu, X. Chen, I.-W. Hsieh, E. Dulkeith, W. M. Green, and Y. A. Vlasov, "Engineering nonlinearities in nanoscale optical systems: physics and applications in dispersion-engineered silicon nanophotonic wires," Adv. Opt. Photon. **1**, 162-235 (2009).

12. H. K. Tsang, C. S. Wong, T. K. Liang, I. E. Day, S. W. Roberts, A. Harpin, J. Drake, and M. Asghari, "Optical dispersion, two-photon absorption and self-phase modulation in silicon waveguides at 1.5 μm wavelength" Appl. Phys. Lett. **80**, 416–418 (2002).
13. A. D. Bristow, N. Rotenberg, H. M. Van Driel "Two-photon absorption and optical Kerr coefficients of silicon for 850 – 2200 nm,", Appl. Phys. Lett. **90**, 191104-191107 (2007).
14. X. Liu, J. B. Driscoll, J. I. Dadap, R. M. Osgood Jr., S. Assefa, Y. A. Vlasov, and W. M. J. Green, "Self-phase modulation and nonlinear loss in silicon nanophotonic wires near the mid-infrared two-photon absorption edge," Opt. Express **19**, 7778-7789 (2011).
15. X. Liu, R. M. Osgood Jr., Y. A. Vlasov, and W. M. J. Green, "Mid-infrared optical parametric amplifier using silicon nanophotonic waveguides," Nat. Photonics **4**, 557–560 (2010).
16. R. K. W. Lau, M. Menard, Y. Okawachi, M. A. Foster, A. C. Turner-Foster, R. Salem, M. Lipson, and A. L. Gaeta, "Continuous-wave mid-infrared frequency conversion in silicon nanowaveguides," Opt. Lett. 36, 1263-1265, (2011).
17. S. Zlatanovic, J. S. Park, S. Moro, J. M. C. Boggio, I. B. Divliansky, N. Alic, S. Mookherjea, and S. Radic, "Mid-infrared wavelength conversion in silicon waveguides using ultracompact telecom-band-derived pump source," Nat. Photonics **4**, 561–564 (2010).
18. G. Crowder, "Infrared methods for gas detection", in Mid-infrared semiconductor optoelectronics, Springer (2006).
19. N. C. Panoiu, X. G. Chen, and R. M. Osgood Jr., "Modulation Instability in Silicon Photonic Nanowires." Opt. Lett. **31**, 3609-3611 (2006).
20. X. Liu, B. Kuyken, G. Roelkens, R. Baets, Y. Vlasov, R. M. Osgood Jr., W. M. J. Green, "Mid-infrared broadband modulation instability and 50dB Raman assisted parametric gain in silicon photonic wires," in CLEO, CTuS2.pdf (2011).
21. B. Kuyken, X. Liu, R. M. Osgood Jr., Y. Vlasov, G. Roelkens, R. Baets, W. M. J. Green, "Frequency conversion of mid-infrared optical signals into the telecom band using nonlinear silicon nanophotonic wires," Optical Fiber Communication Conference, OThU4 (2011).
22. V. Raghunathan, D. Borlaug, R. R. Rice, and B. Jalali, "Demonstration of a Mid-infrared silicon Raman amplifier," Opt. Express **15**, 14355-14362 (2007).
23. N. Akhmediev, M. Karlsson "Cherenkov radiation emitted by solitons in optical fibers," Phys. Rev. A **51**, 2602 (1995).
24. A. Mussot, E. Lantz, H. Maillotte, T. Sylvestre, C. Finot, and S. Pitois, "Spectral broadening of a partially coherent CW laser beam in single-mode optical fibers," Opt. Express **12**, 2838-2843 (2004).
25. J. M. Dudley, G. Genty, F. Dias, B. Kibler, and N. Akhmediev, "Modulation instability, Akhmediev Breathers and continuous wave supercontinuum generation," Opt. Express **17**, 21497-21508 (2009).
26. S. K. Selvaraja, W. Bogaerts, P. Dumon, D. Van Thourhout, and R. Baets, "Subnanometer Linewidth Uniformity in Silicon Nanophotonic Waveguide Devices Using CMOS Fabrication Technology " IEEE J. Sel. Top. Quantum Electron. **12**, 1394–1401 (2006).
27. W. A. Zortman, D. C. Trotter, and M. R. Watts, "Silicon photonics manufacturing," Opt. Express **18**, 23598-23607, (2010).
28. E. Dulkeith, F. Xia, L. Schares, W. M. J. Green, and Y. A. Vlasov, "Group index and group velocity dispersion in silicon-on-insulator photonic wires," Opt. Express, **14**, 3853-3863, (2006).
29. A. C. Turner, C. Manolatou, B. S. Schmidt, M. Lipson, M. A. Foster, J. E. Sharping, and A. L. Gaeta, "Tailored anomalous group-velocity dispersion in silicon channel waveguides," Opt. Express **14**, 4357-4362, (2006).
30. R. Dekker, N. Usechak, M. Forst, and A. Driessen, "Ultrafast nonlinear all-optical processes in silicon-on-insulator waveguides," J. Phys. D: Appl. Phys. **40**, 249–271, (2007).
31. X. Liu, W. M. J. Green, X. Chen, I.-W. Hsieh, J. I. Dadap, Y. A. Vlasov, and J. Osgood, R. M., "Conformal dielectric overlayers for engineering dispersion and effective nonlinearity of silicon nanophotonic wires," Opt. Lett. **33**, 2889-2891, (2008).

1. Introduction

Broadband supercontinuum generation is of great interest for applications such as spectroscopy and optical coherence tomography, where the ultra-broadband and spatially coherent nature of the source can be used to improve measurement throughput and resolution [1, 2]. Within a telecommunications context, a supercontinuum source at telecom wavelengths could be spectrally sliced into numerous WDM channels, and used for short-reach optical links [3]. Supercontinuum generation using photonic crystal fibers has been an area of active research over the past decade [4-6], and has resulted in the commercialization of broadband supercontinuum sources targeting various spectral ranges.

On-chip integrated supercontinuum sources, based upon compact planar waveguide circuits rather than optical fibers, could play a role in reducing the size, power consumption, and cost of instruments and systems targeting the above applications. For example, previous work has exploited the large effective Kerr nonlinearity parameter γ in planar waveguides composed of amorphous chalcogenides [7], silicon nitride [8] or the high-index doped glass Hydex [9], to generate low-threshold power telecom-band supercontinua. Another attractive approach to integrated telecom supercontinuum generation is to utilize the significantly larger nonlinearity possible with crystalline silicon-on-insulator (SOI) wire waveguides [10, 11]. However, the generation efficiency has been limited by silicon's large nonlinear two-photon absorption [12] at telecom pump wavelengths. By working at mid-IR wavelengths near $\lambda \approx$ 2200 nm, where the photon energies are approximately half the band gap energy of silicon, two-photon absorption can be efficiently suppressed [13, 14]. This fact has recently been used to demonstrate highly efficient four-wave mixing-based wavelength conversion and optical parametric amplification of mid-infrared (mid-IR) signals [15- 17]. In this work, we generate a supercontinuum source spanning the wavelength range from 1535 nm to 2525 nm by pumping silicon wires at a wavelength of 2120 nm, thus illustrating that mid-IR pumping may be employed to generate an efficient chip-scale supercontinuum source. Such a broadband infrared supercontinuum source has potential for use in vibrational spectroscopy, as it overlaps the fundamental and higher-harmonic rovibrational absorption lines associated with "fingerprinting" of various molecules [18]. The supercontinuum is generated from picosecond pulses with moderate peak powers, in contrast to previously demonstrated supercontinua in planar waveguide circuits, where high power femtosecond pulses were used [7-9]. The combination of the relaxed pump pulse requirements and the generated supercontinuum spectral range makes the silicon wire waveguide platform attractive for development of highly integrated wideband infrared optical sources.

2. Experimental setup

The silicon photonic wires used are fabricated in a CMOS pilot line, using 200 mm SOI wafers consisting of a 220 nm silicon waveguide layer on a 2 µm buried oxide layer. The wires are 900 nm wide with no top cladding, as shown in the inset of Figure 1. The strong optical confinement resulting from the upper air cladding results in a high effective nonlinearity parameter, and also contributes to anomalous dispersion in the mid-IR. By averaging the nonlinear susceptibility of bulk Si over the electric field of the fundamental TE-polarized waveguide mode, the real part of the nonlinearity parameter is estimated to be γ_{Re} = 150 $(W \cdot m)^{-1}$ [11]. The group velocity dispersion β_2 of the fundamental TE mode is calculated using a commercial finite element mode solver (RSoft FemSim). As shown in Figure 1, the wire exhibits anomalous dispersion ($\beta_2 < 0$) between 1810 nm and 2410 nm.

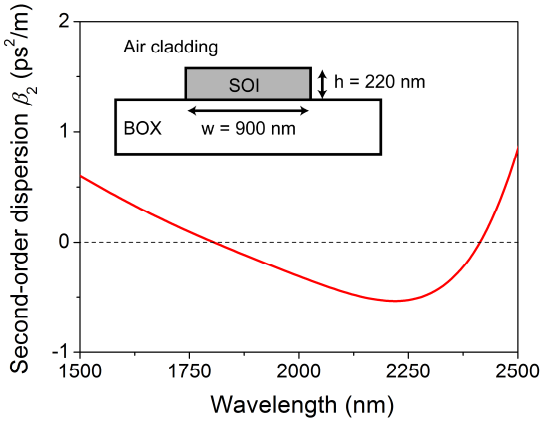

Fig. 1: Group velocity dispersion of the silicon wire waveguide as a function of the wavelength, exhibiting anomalous dispersion ($\beta_2 < 0$) between 1810 nm and 2410 nm. The inset shows the fabricated wire waveguide dimensions.

The supercontinuum generation experiments are conducted using a picosecond pulse train at a center wavelength of 2120 nm as the pump (Coherent Mira-OPO, FWHM = 2 ps, repetition rate = 76 MHz). Using a cut back technique the TE mode waveguide propagation loss is found to be approximately 2.5 dB/cm, across the mid-IR wavelength range from 2050-2450 nm, as well as at wavelengths near 1550 nm. The waveguide used in the supercontinuum experiments is 2 cm in length. The coupling loss at the cleaved input/output facets is 10 dB/facet. The spectrum at the waveguide output is characterized with a mid-IR optical spectrum analyzer (OSA) at a 1 nm resolution.

3. Results

Figure 2 illustrates the evolution of the waveguide output spectrum as the input coupled peak pump power is gradually increased from 3.1 W (green trace) to 12.7 W (black trace). These spectra reveal that a number of different nonlinear processes ultimately combine to produce the broadband supercontinuum. At an input power of 3.1 W, a series of sidebands are generated in the vicinity of the pump at 2120 nm. Closest to the pump, two broad sidebands (labeled as MI(1)) are generated near wavelengths of 1990 nm and 2250 nm. Further away from the pump, a pair of narrowband peaks (labeled as MI(2)) appear at wavelengths of 1870 nm and approximately 2510 nm. Both the broad and narrow sideband pairs originate from modulation instability [19-21], i.e. the amplification of background noise at wavelengths for which the phase matching condition in Eq. (1) below is satisfied.

$$\beta_2 \Delta\omega^2 + \frac{1}{12}\beta_4 \Delta\omega^4 + 2\gamma_{\mathrm{Re}} P = \Delta k_{lin} + \Delta k_{nonlin} = 0 \qquad (1)$$

Here, β_2 and β_4 are the second- and fourth-order waveguide dispersion respectively, $\Delta\omega$ is the detuning of the idler and signal from the pump, γ_{Re} is the real part of the effective nonlinearity parameter, and P is the peak pump power. The modulation instability sidebands appear where the linear phase mismatch $\Delta k_{\mathrm{lin}} = \beta_2\Delta\omega^2 + (1/12)\cdot\beta_4\Delta\omega^4$ and the nonlinear phase mismatch $\Delta k_{\mathrm{nonlin}} = 2\gamma_{\mathrm{Re}}P$ cancel one another. Finally, Figure 2 shows that a Raman Stokes peak appears near 2400 nm, red-shifted by ~15.6 THz from the pump as expected [22].

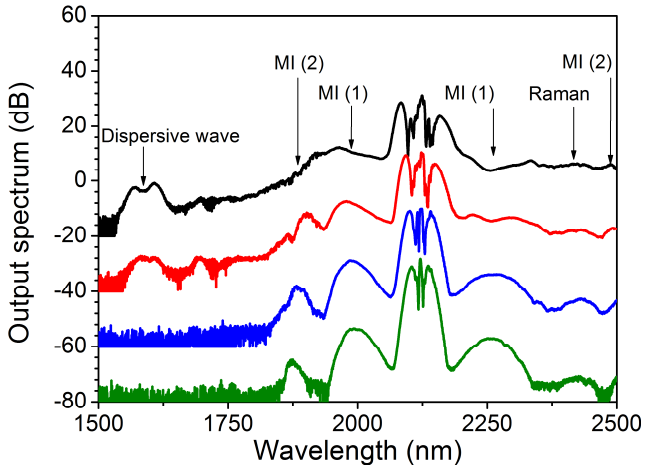

Fig. 2: Measured output spectrum for increasing values of coupled input peak power: 3.1 W (green), 4.3 W (blue), 7.9 W (red) and 12.7 W (black). The spectra are vertically offset by multiples of 20 dB for clarity.

Even at the lowest input power, the pump pulse train's spectrum is broadened significantly by self phase modulation (SPM), as illustrated by the numerous interference fringes appearing near 2120 nm. In turn, this causes associated broadening of the sidebands generated through modulation instability and Raman scattering. When the coupled peak pump

power is increased to 4.3 W, the spectral intensity of the generated sidebands is observed to increase with respect to the pump, and the degree of pump and sideband broadening increases.

At a pump power of 7.9 W, several new spectral components are observed, peaked near 1700 nm and 1600 nm respectively. The term at 1700 nm is generated through cascaded four-wave mixing (FWM), where the original MI(2) peak at 1890 nm serves as the degenerate pump and the input pulse at 2120 nm acts as the signal. The peak around 1600 nm is believed to be the result of Cherenkov radiation referred to as dispersive wave generation [23]. At first sight this is unexpected when we compare the different length scales in our experiment. The nonlinear length is approximately L_{nl} = 500 µm at a coupled peak power of 12.7 W, whereas the soliton fission length is 6.3 cm [5], significantly longer than the wire waveguide's length. Therefore, generation of a dispersive wave through soliton fission is unlikely. However, recent research [24, 25] has shown that in the "long pulse" regime where modulation instability is the main driving force behind supercontinuum generation, dispersive waves can also be generated through the simultaneous formation of pre-solitonic breathers along the pump pulse.

There are several facts supporting this finding. First, the 1600 nm peak lies within the normal dispersion regime of the silicon wire, as expected for the generation of dispersive waves. In addition, there is no combination of the observed modulation instability and/or Raman peaks that can generate the 1600 nm component through cascaded FWM. Moreover, seeding the supercontinuum using a CW laser at 1600 nm does not reveal any parametric gain at this wavelength. This lack of gain excludes the possibility that the 1600 nm component is generated through the process of modulation instability phase-matched through even higher-order dispersion terms (e.g. β_6, β_8), which become important at large detuning from the pump.

Finally, at the highest pump power of 12.7 W, Figure 2 shows that the spectral broadening of all generated peaks leads to the merging of the MI(1), MI(2), and Raman peaks, and to increased flatness of the output spectrum on both the red and blue sides of the pump. Under these conditions, the supercontinuum output from the mid-IR pumped SOI wire waveguide extends from 1540 nm to beyond 2500 nm, the maximum wavelength resolved by the OSA used.

To characterize the presence of any additional spectral components beyond 2500 nm, a Fourier Transform Infrared spectrometer (FTIR) equipped with a liquid nitrogen-cooled InAs detector is used. As shown in Figure 3, the FTIR measurements reveal that the supercontinuum extends to a maximum wavelength of 2525 nm on the red side of the pump. Generation of light at longer wavelengths through modulation instability is not expected because the phase-matching condition in Eq. (1) has no solutions beyond 2525 nm, even when higher-order dispersion terms of the wire waveguide are taken into account (discussed below in Figure 6). While additional weak spectral components could potentially be generated by cascaded FWM, these are not likely to be visible due to the high noise floor of the InAs detector, as well as the limited 38 dB dynamic range of the FTIR A/D converter.

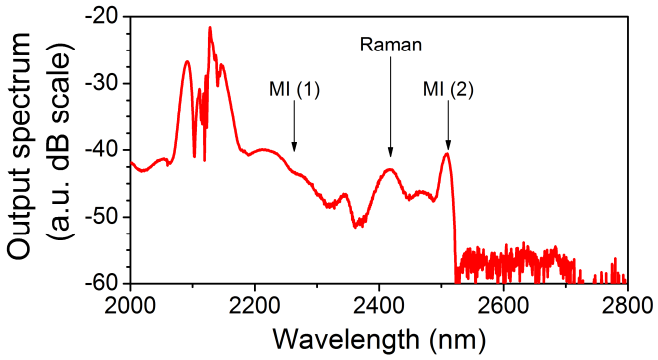

Fig. 3: Output spectrum on the red side of the pump, as measured by FTIR at a coupled input peak power of 12.7 W.

The basic processes contributing to the observed broadband generation can be further understood by characterizing the output spectrum while seeding the supercontinuum at several different spectral locations, as shown in Figure 4. This is accomplished by combining the high-power pump pulse train with a weak (< 0.2 mW) mid-IR CW tunable laser. By comparing the green trace, seeded at 2415 nm close to the Raman Stokes wavelength, with the blue reference curve, which illustrates the unperturbed supercontinuum, the injected seed signal can be seen to experience stimulated Raman amplification at the output of the waveguide. The amplification is demonstrated by the appearance of a strong pedestal at the base of the CW seed line, which is also broadened by cross-phase modulation by the pulsed pump. The red trace, seeded at 2496 nm near the narrowband phase-matching wavelength MI(2), shows that a similar signal amplification pedestal is generated along with a wavelength-converted idler peak at approximately 1880 nm, this time via phase-matched FWM parametric amplification [15]. Moreover, through a cascaded FWM process in which the idler acts as the pump and the 2120 nm pulse train acts as the signal, a second peak at approximately 1690 nm appears.

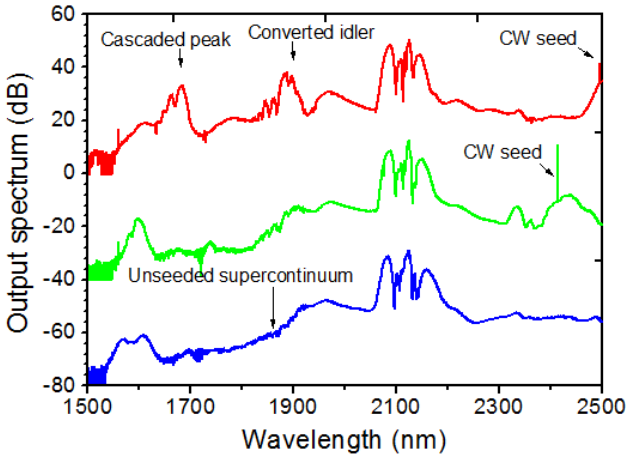

Fig. 4: Measured output spectra obtained while seeding the supercontinuum at a wavelength of 2415 nm (green) and 2496 nm (red), using a CW mid-infrared laser. The blue curve shows the unseeded output spectrum as a reference. The coupled peak power is 12.7 W in all cases. The spectra are vertically offset by multiples of 40 dB for clarity.

Through analysis of several experiments in which the seed signal is tuned over the range 2200-2500 nm, the on-chip gain and conversion efficiency occurring across the supercontinuum are quantified in Figure 5, following the approach applied in [15]. Strong signal amplification (red circle symbols, as large as 31 dB) occurs within the pump's Raman Stokes band (hatched), centered around 2375 nm. However, the absence of wavelength conversion gain (black square symbols, less than 0 dB observed in experiment) within the associated anti-Stokes band near 1910 nm indicates that phase-matching is not preserved between the MI(1) and MI(2) peaks seen in Figure 2, and that Raman scattering is not coherently reinforced within the supercontinuum. In contrast, Figure 5 illustrates that within both the MI(1) regions (2200-2300 nm) closest to the pump and the MI(2) regions (2387-2500 nm) beyond the hatched Raman band, phase-matching leads simultaneously to efficient wavelength conversion and parametric signal gain, ranging from 18-30 dB. These observations illustrate that the supercontinuum is generated primarily through broadband amplification of noise, both with and without phase-matching. As discussed previously, this conclusion is in agreement with what one would expect from the "effective optical length

scales" involved within the SOI wire. Because the soliton fission length is significantly longer than the length of the wire waveguide, soliton fission is unlikely to occur and the supercontinuum is predictably dominated by modulation instability and Raman scattering.

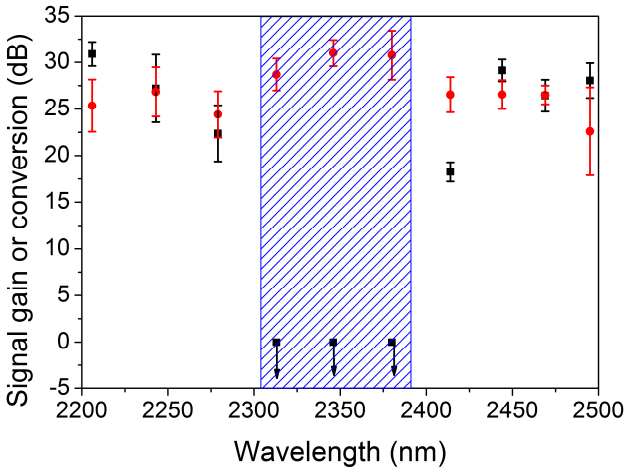

Fig. 5: On-chip signal gain (red dots) and wavelength conversion efficiency (black squares) at a peak power of 12.7 W as measured through seeding the supercontinuum at various wavelengths. The hatched areas label the pump's Raman Stokes and matching anti-Stokes bands.

4. Analysis of phase mismatch and waveguide dispersion

The experiments described above illustrate that in addition to contributions from Raman scattering and dispersive waves, the supercontinuum generation is largely dominated by the phase-matched process of modulation instability. Aside from the dispersive wave peak appearing near 1600 nm, Figure 2 and Figure 3 show that the supercontinuum bandwidth is spanned by the phase-matched MI(2) peaks near 1870 nm and 2510 nm. Therefore, in order to understand how to further increase the bandwidth and intensity of the supercontinuum, additional analysis of the wavelength-dependent phase mismatch around the pump, and the associated dispersion coefficients β_2 and β_4, is required.

Although we do not have direct experimental access to the value of the linear phase mismatch $-\Delta k_{lin}$, Eq. (1) illustrates that an estimate can be generated using the nonlinear phase mismatch term $\Delta k_{nonlin} = 2\gamma_{Re}P$, because the linear and nonlinear phase terms are equal and opposite in sign where efficient MI occurs. Furthermore, the detuning frequencies $\Delta\omega$ where Eq. (1) is satisfied for different values of input peak pump power can be read directly from locations of the MI peaks in Figure 2. The experimental nonlinear phase mismatch values can then plotted versus their respective detunings as shown in Figure 6. By fitting this data, an estimate of the linear phase mismatch $-\Delta k_{lin}$ around the pump is generated.

However, when evaluating the nonlinear phase mismatch term $2\gamma_{Re}P$, it is important to account for the fact that the pump power decreases along the length of the waveguide, due to both linear and nonlinear loss from residual two-photon absorption (TPA). As a result, the nonlinear MI process will get weaker with propagation length. The majority of the observable MI (and nonlinear phase shift) will in fact originate near the input end of the waveguide. For this reason, the nonlinear phasematch is estimated using an "average" value of the peak pump power calculated along the entrance portion of the waveguide, where the power remains larger than $1/e$ of the coupled power P_0 at the input facet. The average power $P_{avg1/e}$ is calculated by solving Eq. (2) and Eq. (3) below.

$$P_{avg\,1/e} = \frac{1}{z_{1/e}} \int_0^{z_{1/e}} P(z)\,dz \qquad (2)$$

$$\frac{dP}{dz} = -\alpha P - 2\gamma_{\mathrm{Im}} P^2 \qquad (3)$$

Here, α is the linear loss of the waveguide (0.58/cm), γ_{Im} (6.3 $(\mathrm{W\cdot m})^{-1}$) is the imaginary part of the waveguide's effective nonlinear response from two-photon absorption, and $z_{1/e}$ the length after which the power has dropped by $1/e$. Due to the short duration of the pump pulses and the small TPA coefficient, the effect of TPA-induced free carrier absorption is miniscule and can be neglected.

The red squares in Figure 6 are then located by plotting the nonlinear phase mismatch $2\gamma P_{avg1/e}$ versus the detuning $\Delta\omega$ for MI bands on the red side of the pump. The uncertainty in the magnitude of the nonlinear phase shift (vertical error bar) is derived from a 1 dB uncertainty in the determination of the input coupling loss, and therefore increases with increasing pump power. The uncertainty in the detuning (horizontal error bar) is derived from the -1 dB bandwidth of the modulation instability peaks in Figure 2. As the experimental data points in Figure 6 correspond to spectral positions at which the linear and nonlinear phase mismatch are equal and opposite in sign, a fit curve drawn through the data following the form of Eq. (1) will therefore yield $-\Delta k_{lin}(\Delta\omega)$, and can thus be used to obtain an experimental estimate of β_2 and β_4. The solid black line in Figure 6 depicts the fit for $-\Delta k_{lin}(\Delta\omega)$ obtained by using a regression technique to minimize the left hand side of Eq. (1). The shaded region illustrates the bounds on the fitted detuning curve resulting from the error on the dispersion coefficients.

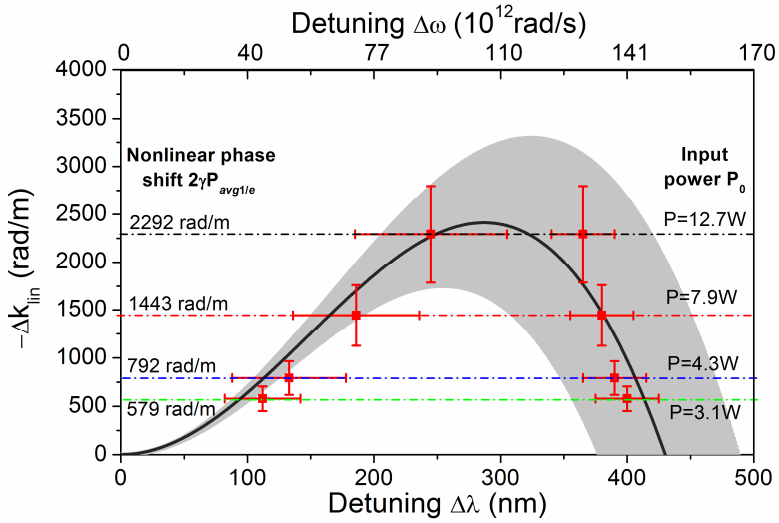

Fig. 6: Curve fit describing the linear phase mismatch after propagation through the 2 cm long waveguide, as a function of detuning on the red side of the pump. The silicon wire dispersion coefficients extracted from this fit are $\beta_2 = -0.43 \pm 0.07$ ps^2/m and $\beta_4 = 2.3 \pm 0.4 \times 10^{-4}$ ps^4/m. The red squares represent the detuning wavelengths of the MI(1) and MI(2) peaks, where the corresponding nonlinear phase mismatch $2\gamma P_{avg1/e}$ term (dash-dotted lines labeled on the left) balances the linear phase mismatch at each value of input peak pump power (labeled on the right). The vertical error bars originate from a 1 dB uncertainty in the input coupling, while the horizontal error bars are associated with the 1 dB bandwidth of each modulation instability peak.

Table 1: Experimental fit and simulated values of the β_2 and β_4 dispersion coefficients associated with the 900-nm wide silicon wire waveguide.

	Fit value	Simulated value
β_2	-0.43 ± 0.07 ps^2/m	-0.47 ps^2/m
β_4	$2.3 \pm 0.4 \times 10^{-4}$ ps^4/m	3.2×10^{-5} ps^4/m

The estimated values for β_2 and β_4 (and their associated standard deviations) from the fit are listed in Table 1. The fit results in a value of -0.43 ± 0.07 ps^2/m for β_2, and $2.3 \pm 0.4 \times 10^{-4}$ ps^4/m for β_4. The fitted dispersion coefficients are also compared to values obtained from numerical mode-solver simulations (Figure 1). The fitted value for β_2 agrees within error to the value of -0.47 ps^2/m predicted by simulations. However, the simulated value for β_4 of 3.2×10^{-5} ps^4/m is approximately a factor of 7 smaller than the fitted value. Unfortunately, small variations in β_4 have a large impact in terms of predicting the conditions for phase matching, particularly because the β_4 dependence in Eq. (1) varies as the fourth power of the detuning $\Delta\omega$. For example, substituting the simulated β_2 and β_4 values into Eq. (1) would suggest that the MI(2) band at the red edge of the supercontinuum in Figure 3 should appear approximately near 3900 nm, which is inconsistent with the experimental observations.

One likely source of the difference between simulated and fitted dispersion coefficients is numerical error. For example, the fourth-order dispersion coefficient β_4 is computed by taking four derivatives of the frequency-dependent modal propagation constant $\beta_0(\omega)$, with numerical uncertainty accumulating at each derivative. However, even if the numerical precision of the mode solver calculations were improved, there will remain more fundamental sources of uncertainty associated with small local variations in the dimensions of the wire waveguide. While the dimensions of a simulated waveguide are assumed to remain constant along its entire length, in practice, the height and width of the core can vary locally due to very small manufacturing variations in the thickness of the SOI layer, lithographic tolerances, and reactive ion etch loading and bias [26, 27]. Various studies have documented that the dispersion of silicon photonic wires is extremely sensitive, even to nanometer-scale variations in their cross-sectional dimensions [28-31], on account of their large refractive index-contrast. While it is possible to control the variation of the waveguide dimensions on the level of a few nanometers using state-of-the-art silicon CMOS processing technology [26, 27], the remaining fluctuations can nevertheless produce significant variations in the dispersion characteristics, particularly in higher-order coefficients such as β_4. Thus, it is important to note that the β_2 and β_4 values derived from the experimental data in fact represent an "average" waveguide dispersion, which takes into account the inevitable manufacturing-dependent local dispersion variations seen by the pump pulses propagating along the 2 cm long waveguide. Moreover, given the difficulty of achieving perfectly uniform dispersion throughout a silicon photonic wire, it is likely that an experimental approach for extracting "average" dispersion values, such as the method outlined above, will be required in combination with numerical simulations to produce a sufficiently accurate design and analysis methodology for broadband highly nonlinear silicon photonic wire devices.

5. Conclusions

In summary, we have shown that a supercontinuum with a bandwidth of nearly 1000 nm spanning from the telecom band to the mid-IR, can be generated by pumping a 2 cm long SOI wire waveguide with mid-IR picosecond pump pulses having moderate peak power. More generally, our demonstration illustrates that when using pump photons with energy close to half the band gap of silicon, SOI wires have an enormous potential as efficient, compact nonlinear optical devices. In addition, we report a valuable method for analysis of the modulation instability peaks within the supercontinuum spectrum, and use this method to re-construct the linear phase-mismatch near the pump as a curve fit to the experimental data. In

turn, the linear phase-mismatch is used to extract values for the dispersion coefficients β_2 and β_4. This method is general and can be applied to characterize the dispersion characteristics of various highly-nonlinear optical devices, based upon silicon or other high-index contrast materials. Comparison of the extracted dispersion values with those obtained through numerical simulations illustrates that the experimental analysis approach can be more accurate, particularly for higher orders of dispersion. In practice, a combination of the experimental and simulation techniques will likely be required for sufficiently accurate silicon nonlinear waveguide device design.

Acknowledgements

The authors would like to thank Prof. Stephane Coen of the University of Auckland and Prof. John Dudley of the University of Franche-Comté for their assistance in the interpretation of the observed supercontinuum spectra, and Yurii A. Vlasov of IBM Research for his constructive technical advice. B. Kuyken acknowledges the Flemish Research Foundation, Vlaanderen for a doctoral fellowship. This work was partly carried out in the framework of the Methusalem "Smart Photonic Chips," FP7-ERC-INSPECTRA and FP7-ERC-MIRACLE.